Optics & Laser Technology 182 (2025) 112191

Contents lists available at ScienceDirect

Optics and Laser Technology

journal homepage: www.elsevier.com/locate/optlastec

Full length article

Effects of different interlayer bonding modes on the microstructure and properties of laser cladded In625

Yingying Zhang, Jiayu Sun, Zhengyu Sun, Yiqi Wang, Tianbiao Yu *

School of Mechanical Engineering and Automation, Northeastern University, Shenyang 110819, China

ARTICLE INFO

Keywords:
Laser cladding
Interlayer bonding mode
In625 alloy
Microstructure
Mechanical property

ABSTRACT

In this study, the effects of five different interlayer bonding modes on the microstructure, mechanical properties, friction, and wear resistance of In625 laser cladding were investigated. XRD, EDS, tensile, hardness, friction and wear tests were conducted. XRD analysis results have revealed that Nb_6C_5 was detected in rectangular ring mode and the long, wide and rectangular ring overlay mode, indicating that the rectangular ring mode may promote the formation of secondary phase. EDS analysis has indicated a slightly higher Nb content in the rectangular ring mode, while the long and wide direction overlay mode exhibited a more uniform grain distribution and smaller grain size. Tensile tests revealed ductile fractures in the long direction, wide direction, the long and wide direction overlay modes, while the rectangle ring mode and the long, wide, and rectangular ring overlay modes showed brittle fractures. The long and wide direction overlay mode had the highest average elongation (35.46 %), and the long, wide, and rectangular ring overlay mode had the highest tensile strength (957.13 MPa). Hardness test results showed that the rectangle ring mode had the highest hardness (325.1 HV (0.2)). Friction and wear tests indicated that the long and wide direction overlay mode exhibited the smallest wear volume (0.08899 mm^3) and the best overall friction performance. These findings indicate that the properties of the cladding layer can be effectively tailored by selecting appropriate interlayer bonding modes to match the specific material requirements in distinct application scenarios.

1. Introduction

Laser cladding (LC) is favored for machine parts repair and functional claddings due to its low dilution, minimal heat-affected zone, and strong metallurgical bonding [1]. It shows great potential in improving material properties and realizing customized manufacturing [2,3]. Existing studies have explored the effect of different process parameters such as power, scanning speed, and powder flow rate on the properties of the cladding layer. Chen et al. [4] used LC to prepare Ni-base cladding and optimized the process parameters. The optimized cladding parameters can increase the microhardness of the cladding to 520 HV0.3, which is about 2.5 times that of the substrate. Yu et al. [5] used the Taguchi grey correlation method to optimize the laser power, scanning speed, and powder feeding speed and selected the optimal process parameter combination with the maximum cladding layer width of 1107.63 μm, the minimum cladding layer height of 276.74 μm and the dilution rate of 38.65 %. Zhang et al. [6] using RSM and NSGA-II, this study optimized laser cladding parameters for Fe-based alloy on Q345B steel, achieving superior cladding performance with 990 W laser power, 381 mm/min scanning speed, and 0.65 r/min powder feed rate. Weng et al. [7] Co-based composite claddings, produced by laser cladding, significantly improved the microhardness and wear resistance of Ti-6Al-4 V titanium alloy. Optimized laser process parameters further enhanced these properties. Xi et al. [8] used YCF102 high-strength weal-resistant alloy powder to prepare a covering layer on the steel substrate by laser cladding technology, established a relationship model of deposition Angle, covering layer width and cladding area, and calculated the dilution rate through the cladding layer and melting area. The proposed theoretical model provided a basis for the estimation of dilution rate in laser cladding. Bourahima et al. [9] used a 4 kW continuous laser to clad Ni-based powder on Cu-Ni-Al substrate, studied the effects of laser power, scanning speed, and powder feeding rate on cladding geometry and bonding quality, and used the ANOVA method to optimize process parameters to improve cladding quality

42CrMo is widely utilized due to its excellent toughness, impact resistance, and superior fatigue performance. However, its corrosion resistance in high-temperature or corrosive environments is relatively poor [10]. In625, a solid-solution strengthened nickel-based superalloy,

* Corresponding author.
E-mail address: tianbiaoyudyx@gmail.com (T. Yu).

https://doi.org/10.1016/j.optlastec.2024.112191
Received 16 June 2024; Received in revised form 15 November 2024; Accepted 20 November 2024
Available online 26 November 2024

is enhanced by the addition of molybdenum and niobium, which impart high strength, as well as excellent corrosion resistance and high-temperature stability [11]. By laser cladding In625 powder onto a 42CrMo substrate, the performance of 42CrMo in high-temperature and corrosive environments can be improved, effectively addressing its limitations under these conditions. Laser cladding of In625 has been extensively studied [12,13], particularly for its critical applications in extreme environments such as those found in aero-engines and nuclear reactors [14]. Rafiei et al. [15] used the finite element method and the moving mesh method to simulate the cladding process of WC/In625 composite material, evaluating the cladding performance, and using the Taguchi experimental design method and linear regression model to study and optimize the effects of process parameters on dilution rate, cladding geometry, heat, and stress. Xu et al. [16] prepared the TiC-enhanced In625 composite cladding by cladding with 4000 W fiber laser, and the study showed that the microhardness, tensile strength, and corrosion resistance of the cladding were significantly improved under appropriate cladding process parameters. Su et al. [17] first used a four-beam coaxial wire-feeding laser cladding system to study the effects of ZrC and CNTs reinforcement particles on the microstructure, mechanical properties, and corrosion resistance of In625 cladding. The results showed that the addition of reinforcement particles significantly improved the mechanical properties and corrosion resistance of the cladding. Wang et al. [18] prepared In625 cladding on Q245R steel substrate by high-speed laser cladding and found that the microstructure and performance of the cladding were different at different scanning speeds, and the cladding at 2 m/min showed the best high-temperature wear resistance.

However, the interlayer bonding modes have a significant impact on the properties of the final cladding layer, especially on the microstructure and mechanical properties of the material [19,20]. Yu et al. [21] studied the effect of different deposition modes (fractal, offset, and grating) on part deformation, internal quality, and mechanical properties in the LSF process by applying fractal deposition mode. The results showed that fractal deposition mode can minimize part deformation and put forward strategies to improve part quality. Wang et al. [22] successfully fabricated oblique thin-walled parts of AISI316L stainless steel by using DLF technology and studied the deposition strategy, microstructure, and mechanical properties. The results showed that the parallel deposition method was more suitable for manufacturing oblique thin-walled parts. Paydas et al. [23] studied the preparation of Ti-6Al-4 V deposition layers with variable thickness using laser cladding to evaluate their application as a remediation technique and studied the influence of construction strategy (BS) and incident energy (IE) on the metallurgical characteristics of the deposition layer. X et al. [24] established 12 kinds of ring cross-scanning strategy models for laser cladding of radial grooves of ring thin-walled parts, carried out thermo-mechanical coupling simulation to study the temperature, stress, and deformation under different scanning strategies, and finally determined the scanning strategy with minimum deformation. Zhao et al. [25] laser-clad Ni204 cladding on the surface of 45# steel alloy significantly improved microhardness and wear resistance by adjusting microstructure evolution and properties through overlapping modes. Yang et al. [26] studied the relationship between the forming shape of a 3D laser-forming metal sheet and process parameters. Nd: YAG laser was used to conduct experimental research on stainless steel 1Cr18Ni9Ti sheet, and the results showed that the cross spider scanning strategy could form the square and round sheet into a spherical dome, and the radial line scanning strategy could form the rectangular sheet into a saddle. Petrat et al. [27] study investigate the influence of different zigzag and spiral strategies on temperature distribution using laser metal deposition (LMD), emphasizing the importance of developing and selecting build-up strategies for different part geometries in LMD.

Systematic research on the impact of inter-layer lap modes on the performance of the cladding layer is still lacking in existing literature, despite some studies on this topic in the laser cladding process. The interlayer bonding modes play a crucial role in determining the thickness, compactness, and grain structure of the cladding layer, consequently influencing the material's hardness, wear resistance, and tensile strength. Different interlayer bonding modes can result in different cooling rates of the fused cladding resulting in differences in the internal temperature of the material, subsequently impacting the overall performance of the cladding. Therefore, this study aims to comprehensively compare the effects of five different interlayer lap modes on laser cladding In625. By utilizing techniques such as scanning electron microscope (SEM), X-ray diffraction (XRD), tensile test, hardness test, and friction and wear test, the specific influences of different interlayer bonding modes on the microstructure, mechanical properties, and wear resistance of the cladding layer were thoroughly examined. The findings of this research not only establish a scientific foundation for enhancing laser cladding technology but also offer technical backing for the utilization of In625 and other high-performance materials in demanding application scenarios.

2. Experimental method

42CrMo substrate size 100 mm × 100 mm × 10 mm. The elemental composition was 0.38–0.45 wt% C, 0.9–1.2 wt% Cr, 0.15–0.25 wt% Mo, 0.5–0.8 wt% Mn, 0.17–0.37 wt% Si, with the balance being Fe. The deposited powder used was In625 spherical powder, with a particle size of 82.39 ± 16.2 μm. The EDS elemental composition and particle size statistics were depicted in Fig. 1. Before the experiment, the substrate was polished with sandpaper and cleaned to remove any oil or impurities present on the surface. The powder was then placed in a 110 °C drying box for 2 h to dry.

The experimental setup consists of an open-loop controlled coaxial powder feeding system, as depicted in Fig. 1. In this study, the length and width of the single cross-section of the cladding layer are 1091 μm and 241 μm, the depth of the molten pool is 99 μm, the overlap rate is 33 %, and the Z-axis lifting is 180 μm. The specific process parameters are shown in Table 1. The trajectories were generated by the offline programming software RobotArt and imported into the control system. The KUKA robot then recognizes and executes these trajectories. The overlay paths, bonding methods, and specimen dimensions are shown in Fig. 2. Path1 represents a serpentine trajectory in the long direction, Path2 represents a serpentine trajectory in the wide direction, and Path3 represents a ring of a rectangle. B1 corresponds to the interlayer bonding mode for Path1, B2 corresponds to the interlayer bonding mode for Path2, B3 corresponds to the interlayer bonding mode for Path1 and Path2, B4 corresponds to the interlayer bonding mode for Path3, and B5 corresponds to the interlayer bonding mode for Path1, Path2, and Path3. No. 1, No. 2, and No. 3 serve as tension specimens for each sample. No. 4 is for SEM and hardness testing, while No. 5 is for XRD and friction-wear testing. The overlayed specimens were obtained through wire cutting, and the measured surfaces of the specimens were sanded and polished before being etched with aqua regia for 15–25 s. XRD analysis was conducted using a Rigaku SmartLab diffractometer. The measurement conditions were set as follows: 45 kV, 200 mA, with a wavelength of 1.541 Å, utilizing a copper target. The microstructure was observed with an Olympus microscope. The fracture morphology and microstructural analysis were performed using a Zeiss Ultra PLUS scanning electron microscope. Tensile tests were conducted on a WDW-100E universal testing machine at a tensile speed of 0.5 mm/min. Hardness tests were carried out with an MH-500 microhardness tester, with measurements taken along the direction of the cladding layer starting from the melt pool. Indentations were spaced 300 μm apart, with a load of 200 kg and a holding time of 10 s. Each height was measured three times, and the average value was reported as the microhardness of the cladding layer. The friction and wear tests were carried out using MFT-4000 multi-functional material surface performance tester, with a load of 15 N, a reciprocating stroke of 5 mm, a sliding speed of 220 mm/min, and a sliding duration of 40 min. The counter material was an Al_2O_3 ball with

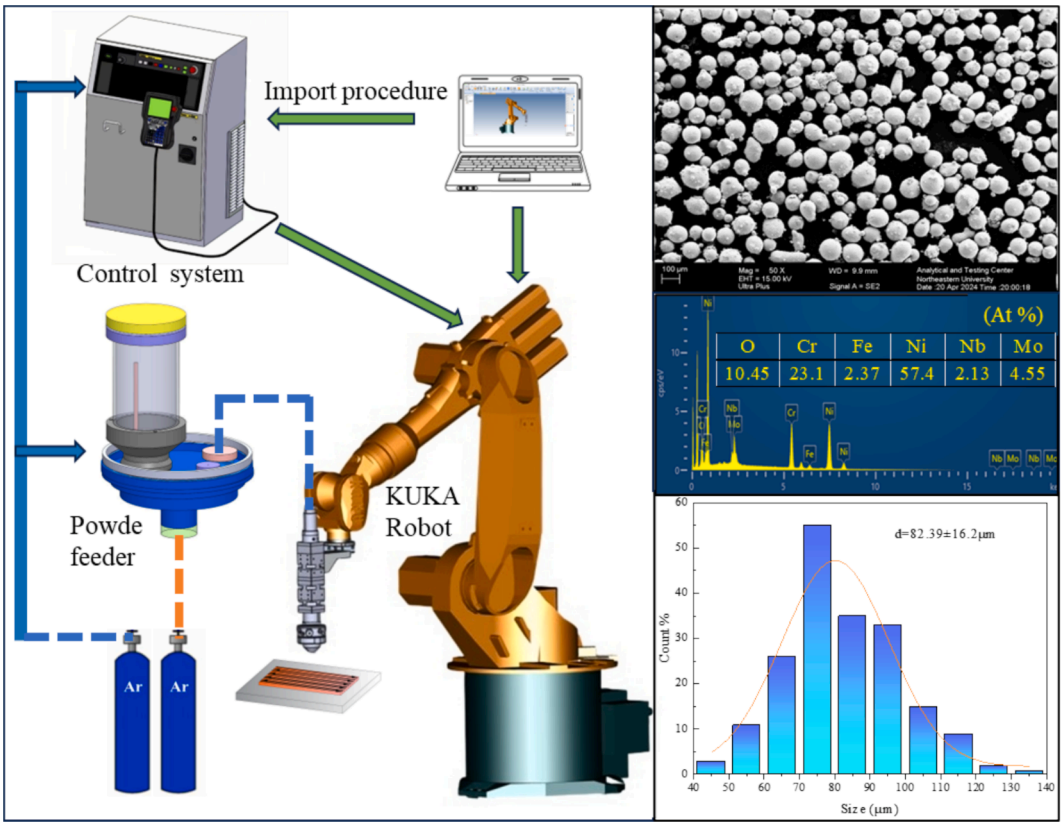

Fig. 1. Laser cladding preparation process and morphology of deposited material.

Table 1
Process parameter.

Process parameter	Value
Laser power (W)	450
Scanning speed (mm/s)	9
Powder feeding rate (g/min)	10.21
Track spacing (mm)	0.73
Z axis increasing (mm)	0.18
Sending powder gas (L/min)	8
Shielding gas (L/min)	15

a diameter of 5 mm and a hardness of 90 HRC (~900 HV).

3. Results and Discussion

3.1. Microstructure

The XRD patterns of the five claddings are shown in Fig. 3. XRD analysis indicated that the five claddings were primarily composed of In625 and γ-Ni solid solutions in an FCC structure [28]. B1 showed only one distinct (111) peak, suggesting a strong preferential alignment along this crystallographic plane. B2 exhibited a strong (111) peak, along with weaker (200) and (220) peaks, which are characteristic of the FCC structure. B3 revealed prominent (200) peaks, with weaker (111) and (220) peaks, which differed from B1 and B2. This difference may be due to the alternating interlayer bonding mode in the long and wide directions, promoting different preferred crystallographic planes. B4 showed stronger (111), (200), and (220) peaks, as well as weaker (131) peaks, with [Nb_6C_5] diffraction peaks detected. Variations in cooling rates during solidification may have contributed to the formation of the [Nb_6C_5] phase in this sample. B5, a combination of Path1, Path2, and Path3, was similar to B4 but with weaker (200), (131), and (111) peaks, as well as weaker [Nb_6C_5] diffraction peaks. Notably, Sample B5′s [Nb_6C_5] peak intensity is lower than that of B4, suggesting a potential attenuation of secondary phase precipitation in the interlayer bonding mode characterized by long and wide directions.

Fig. 4 shows the EDS spectra of the cladding layers under different interlayer bonding modes, and Fig. 5 presents the grain length statistics. The longer the path of each pass, the longer the cooling time; however, with a faster cooling rate, the grain size becomes smaller. Previous researchers enhanced the cooling rate by adjusting the process parameters, which also refined the grain size [29]. Since B2 follows a wide direction path with the shortest path length per pass, the cooling time for the melt pool in the previous pass is minimized, and the process quickly moves to the next cladding pass. Additionally, the overlap zone is cladded again, reducing the overall cooling rate. As a result, the cooling rate for B2 is the slowest, and the grain length is the largest, with most grains exhibiting a honeycomb structure. In contrast, B1, which follows a long direction path, experiences a faster cooling rate than B2, resulting in smaller grains. The grain size is more uniform, and the grains mostly exhibit a honeycomb structure. B4, which uses a ring of a rectangle path, shows variable cooling rates—initially faster and then slower—as the ring-shaped path decreases in size. Consequently, the grain size for B4 is smaller than B2 but larger than B1, with the grain structure predominantly dendritic. B3, which combines both the long direction and wide direction paths, results in the smallest grain length and the most uniform distribution, with most grains exhibiting a dendritic structure. B5, which integrates all three path types, shows a larger temperature gradient, leading to non-uniform grain lengths. The grain structure is predominantly dendritic, with some areas displaying reticulated grains. The EDS elemental distribution results for all samples are shown in Table 2, and it is noteworthy that B4 contains the highest concentration of Nb. When compared with the XRD results, diffraction peaks corresponding to the secondary phase [Nb_6C_5] were detected in both B4 and B5, which may be attributed to the variation in the different interlayer bonding modes.

Fig. 6 illustrates the cross-sectional morphology of the cladding

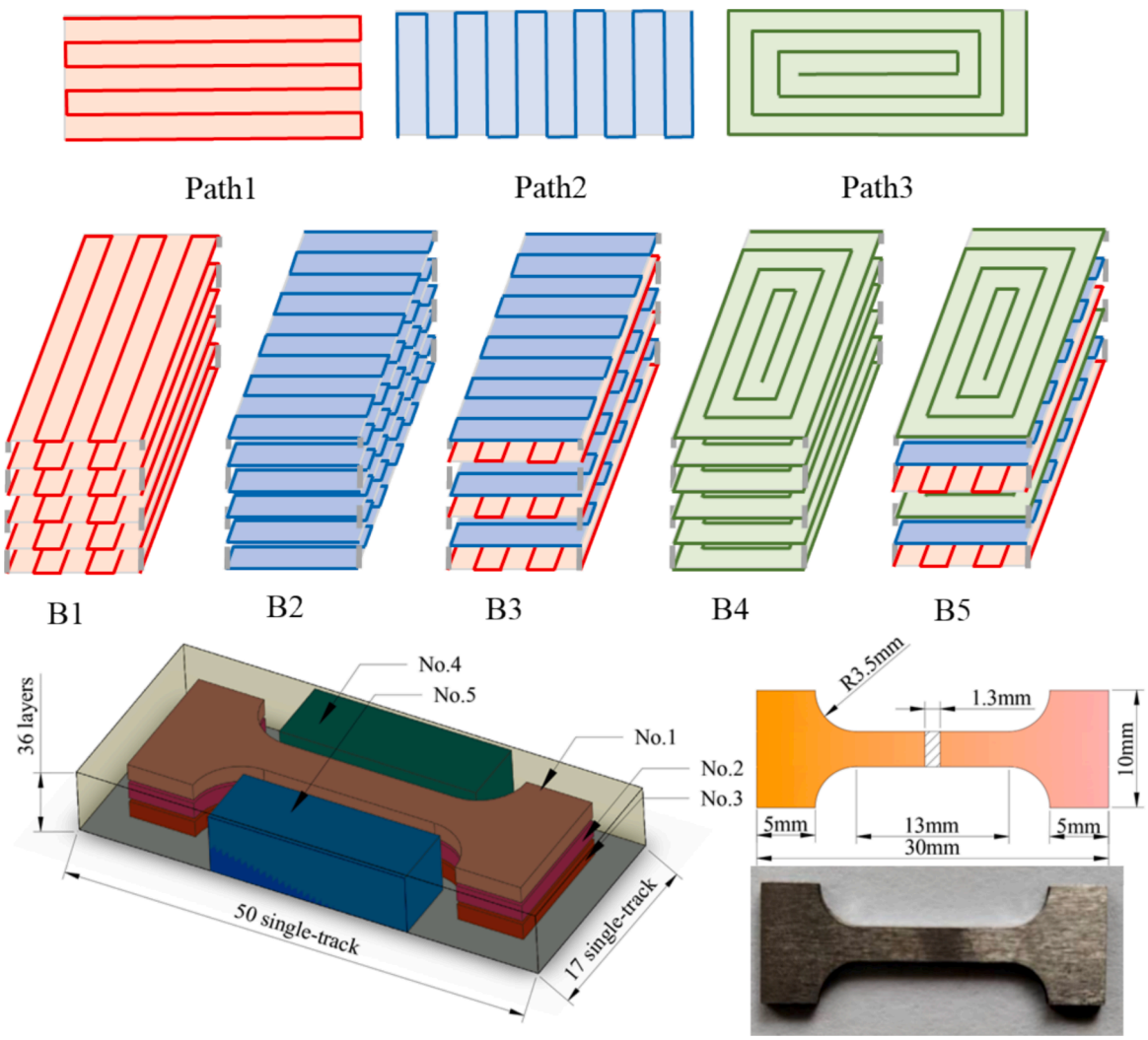

Fig. 2. Description of experimental design.

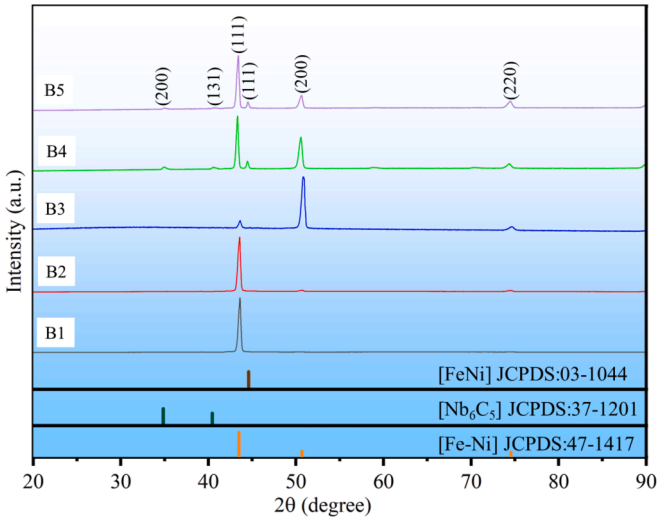

Fig. 3. XRD patterns of the five claddings.

under different interlayer bonding modes, revealing varying degrees of pores and cracks across all samples. The metallurgical bonding quality is generally good in the lap areas of B1–B4, whereas B5 exhibits slag inclusion defects in its lap area. The different interlayer bonding alters the distribution direction of the heat-affected zone, modifying the remelting process and subsequently affecting the temperature of the cladding, which in turn leads to the formation of various defects [19,30]. Among all the samples analyzed, B3 exhibits the fewest pores and cracks.

3.2. *Compressive strength*

Different interlayer bonding modes affect crystallographic plane alignment, grain boundaries, bonding interfaces, and microscopic defects, thereby influencing the material's strength. The engineering stress–strain curves and statistical data of the five claddings are shown in Fig. 7. The fracture morphology of the top layers of the five claddings is presented in Fig. 8. The fracture surfaces of B1 and B2 both exhibit numerous small, evenly distributed dimples, which enhance the material's energy absorption, toughness, and impact resistance [31]. However, the average tensile strength of B1 is higher than that of B2, while the average elongation of B2 exceeds that of B1. This can be attributed to the more orderly alignment of grains in a specific direction for both B1 and B2, allowing the material to exhibit greater strength and toughness along that direction. In contrast, B3 also shows evenly distributed dimples at the fracture surface, further improving its energy absorption, toughness, and impact resistance. Notably, B3 exhibits the highest average elongation (35.46 %), and the average tensile strength is also

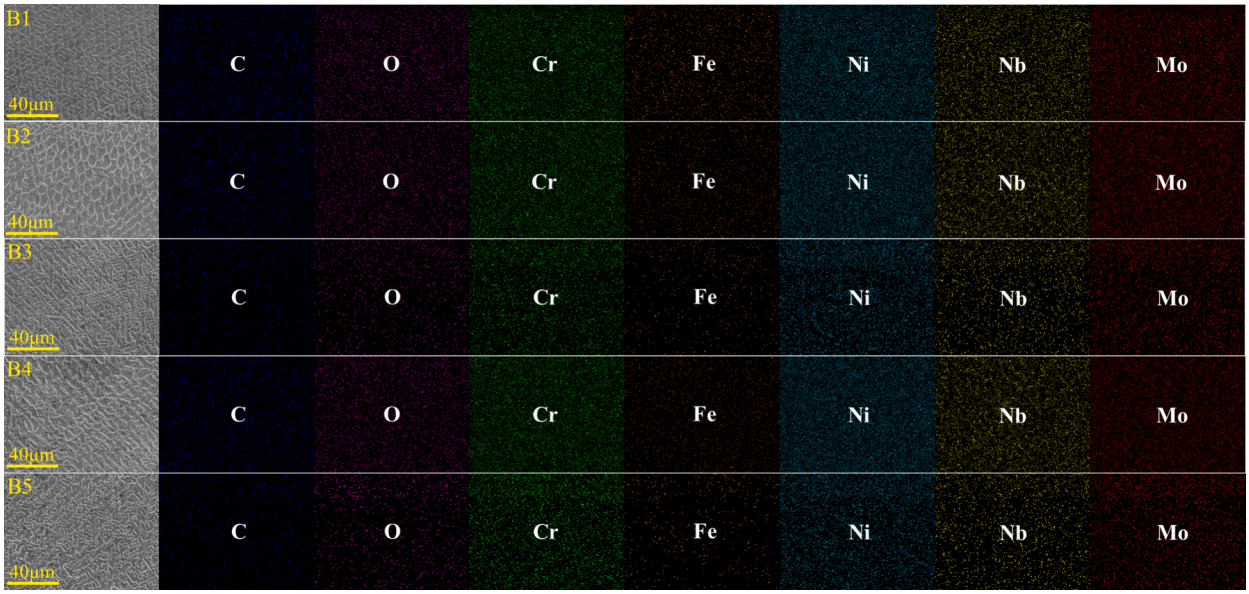

Fig. 4. EDS elemental mapping of the five claddings.

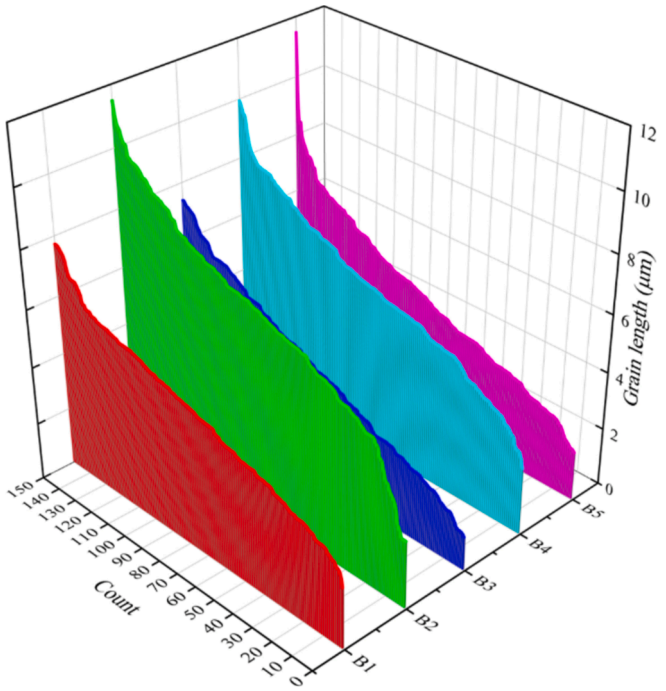

Fig. 5. Statistical chart of grain length of the five claddings.

Table 2
EDS element distribution of the five claddings.

No.	Element (At%)						
	C	O	Cr	Fe	Ni	Nb	Mo
B1	22.52	2.71	19.7	1.13	47.5	2.05	4.36
B2	27.47	2.47	17.9	1.16	44.4	2.81	3.79
B3	26.51	3.76	17.8	1.31	44.5	2.52	3.62
B4	25.66	3.48	17.9	1.35	44.7	2.85	4.03
B5	30.54	2	17.6	1.15	42.6	2.58	3.56

high. This is because B3′s grains grow alternately in the longitudinal and transverse directions, reducing the orientation bias and resulting in more uniform material properties in all directions, thereby minimizing anisotropy. On the other hand, B4 and B5 display typical brittle fracture characteristics, with smooth fracture surfaces and fewer dimples. B5 exhibits the highest average tensile strength (957.13 MPa). Although they have relatively high average tensile strength, their average elongation is very low.

This may be due to the inclusion of a ring of a rectangle path in B4 and B5, which resulted in uneven cooling rates. This, in turn, led to more complex crystallographic plane alignment. Previous researchers have suggested that the existence of these intricate crystallographic plane arrangements within the composite material can lead to brittle fracture characteristics during tensile testing [32]. The tensile tests indicate that different interlayer bonding modes significantly affect tensile strength, elongation, and fracture modes. According to the ASTM B564 standard, compared to forged Inconel 625 material, B1, B3, B4, and B5 meet the minimum tensile strength requirement, but only B2 and B3 satisfy the minimum elongation standard.

3.3. Microhardness

Fig. 9 presents the hardness statistics for the five claddings. The average hardness of B1 is 316.3 HV (0.2), with a gradual increase observed from the melt pool to the cladding. The average hardness of B2 is 301.9 HV (0.2), showing a gradual increase from the melt pool to approximately 300 μm, after which the hardness remains relatively stable. The average hardness of B3 is 316.9 HV (0.2), with a more uniform distribution and minimal fluctuations. B4 exhibits the highest average hardness at 325.1 HV (0.2); however, there is a significant variation in hardness between the melt pool and the top of the cladding layer, leading to an uneven hardness distribution and substantial hardness fluctuations. B5 has an average hardness of 301.4 HV (0.2), with higher hardness at the top of the cladding layer and considerable fluctuations. Combined with the XRD results, the secondary phase [Nb_6C_5] was detected in both B4 and B5 claddings. The highest average hardness was observed in B4, primarily due to the use of only a rectangular ring path, which facilitated the formation of the secondary phase [Nb_6C_5]. According to previous studies, the second phase strengthening can hinder the formation of plastic deformation and wear marks of the cladding and can improve the hardness and wear coefficient of the cladding [33]. In contrast, B5 exhibited the lowest average hardness,

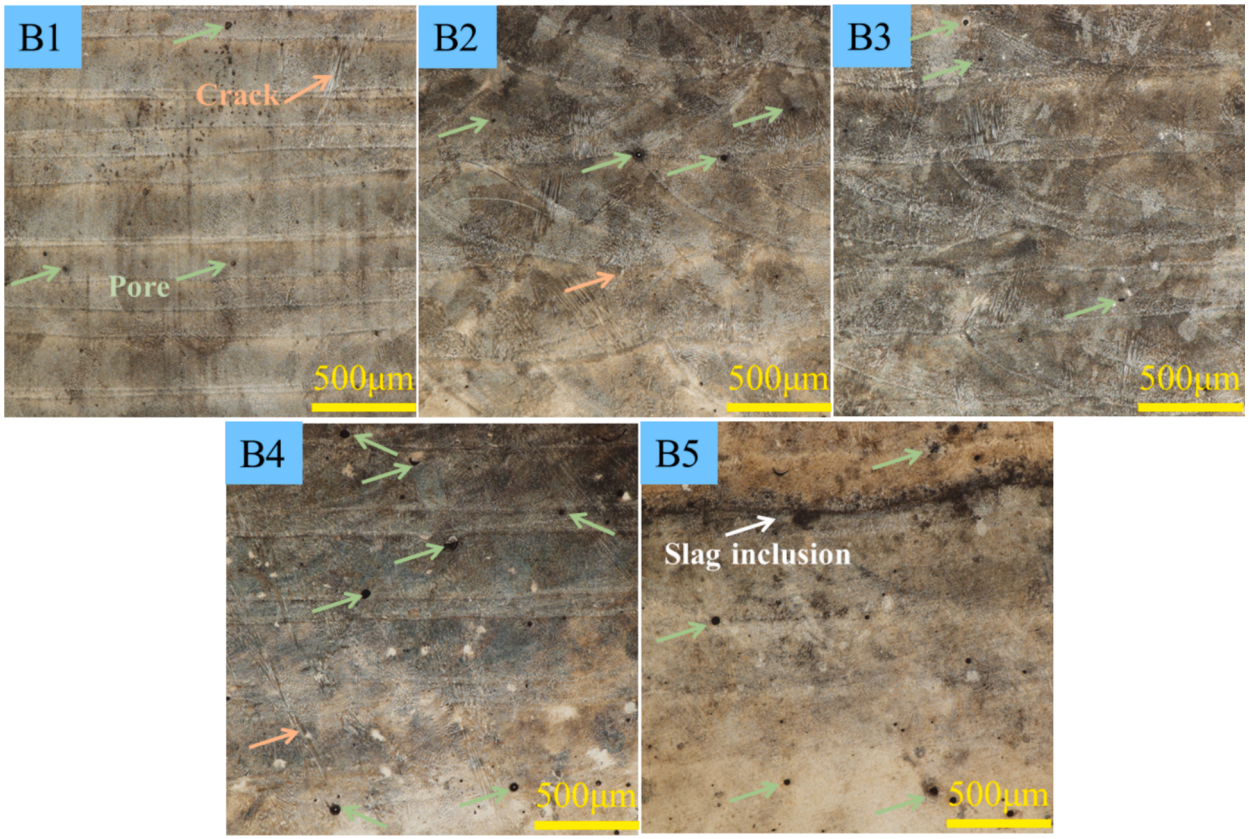

Fig. 6. Cross-sectional morphology of the five claddings.

and the diffraction peaks of the secondary phase [Nb_6C_5] were slightly lower than those in B4. This phenomenon can be attributed to B5′s use of a combination of long, wide, and rectangular ring paths, which resulted in different cooling rates across the cladding layers, leading to a lower average hardness and an uneven hardness distribution.

3.4. Wear resistance

The friction coefficient curves of the five claddings are shown in Fig. 10. At the beginning of the friction and wear experiment, the surfaces of the sample and the grinding ball made initial contact, and the microstructure of the sample surface gradually adapted to the grinding ball surface, entering the adaptive friction stage. After about 5 min, the friction process stabilized and transitioned into the steady-state friction phase. After 10 min, the friction and wear rate between the sample surface and the grinding ball became relatively stable, marking the onset of a stable friction state. The friction coefficients of B4 and B5 were relatively high in the initial stage, primarily due to the instability caused by their internal crystal structures and defects. In the 30–40 min wear stage, the friction coefficient order was as follows: B3 ($\mu = 0.5824$) > B2 ($\mu = 0.5645$) > B5 ($\mu = 0.5482$) > B1 ($\mu = 0.5456$) > B4 ($\mu = 0.5446$). Notably, B4 exhibited the lowest friction coefficient.

Fig. 11 illustrates the wear morphology and EDS analysis results of the five claddings. Typical adhesive wear and abrasive wear features such as ploughing, adhesion, and spalling zones, were observed on the surfaces of the five claddings [34]. EDS analysis subsequently detected the presence of Al elements from the counter-abrasive balls in the wear scars, confirming the occurrence of adhesive wear. The hardness of the claddings was about 310 HV (0.2). A greater difference in hardness between the cladding and the counter-abrasive ball increases the likelihood of adhesive wear. During adhesive wear, material from the cladding surface adheres to the counter-abrasive ball upon contact, and during separation, this adhered material flakes off, resulting in further wear of the cladding surface and negatively impacting the overall wear resistance of the cladding.

Fig. 12 illustrates the wear trajectories, scratch depths, and volume losses for the five claddings. The wear of B1-B5 is 0.09449 mm^3, 0.1127 mm^3, 0.08899 mm^3, 0.11611 $mm^3$and 0.12385 mm^3, respectively. It can be observed that, although B3 has the highest friction coefficient, it exhibits the smallest wear volume. In contrast, B4 and B5 have lower friction coefficients but larger wear volumes. This agrees with the findings of Chen et al. that the coefficient of friction is not directly proportional to the wear rate [35]. When analyzed in conjunction with the results of tensile experiments and hardness tests, B3 demonstrates minimal wear loss, primarily due to its more uniform hardness distribution, better toughness, and fewer defects in the cladding layer. On the other hand, the increased wear volumes in B4 and B5 can be attributed to their uneven hardness distribution and poor toughness. When a material has poor toughness, its surface may initially exhibit a lower coefficient of friction due to smoother surfaces or reduced deformation. However, such materials tend to be more brittle and prone to microcrack formation. During the wear process, these microcracks grow and form larger particles, which subsequently accelerate the wear. Therefore, while the coefficient of friction reflects the sliding resistance between two contact surfaces, it does not directly indicate the material's wear resistance. Instead, wear resistance is more accurately assessed by the amount of material loss. A smaller wear volume suggests that the material has a greater ability to resist wear during sliding friction, leading to superior frictional properties. Hence, B3 exhibits the best overall frictional performance.

4. Conclusions

The effects of five different interlayer bonding modes on the properties of laser cladding In625 were systematically analyzed in this study. It was found that the microstructure, mechanical properties, and wear

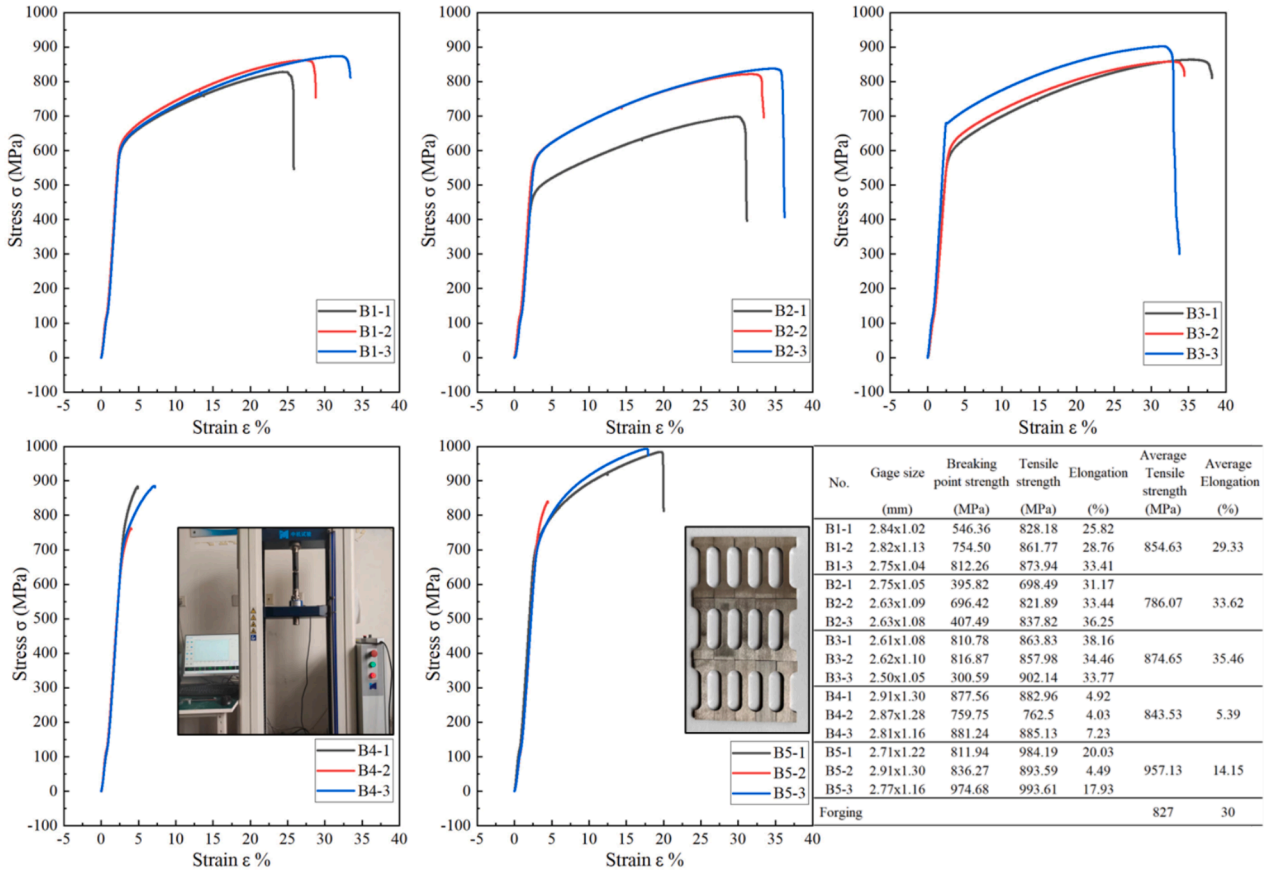

No.	Gage size (mm)	Breaking point strength (MPa)	Tensile strength (MPa)	Elongation (%)	Average Tensile strength (MPa)	Average Elongation (%)
B1-1	2.84x1.02	546.36	828.18	25.82		
B1-2	2.82x1.13	754.50	861.77	28.76	854.63	29.33
B1-3	2.75x1.04	812.26	873.94	33.41		
B2-1	2.75x1.05	395.82	698.49	31.17		
B2-2	2.63x1.09	696.42	821.89	33.44	786.07	33.62
B2-3	2.63x1.08	407.49	837.82	36.25		
B3-1	2.61x1.08	810.78	863.83	38.16		
B3-2	2.62x1.10	816.87	857.98	34.46	874.65	35.46
B3-3	2.50x1.05	300.59	902.14	33.77		
B4-1	2.91x1.30	877.56	882.96	4.92		
B4-2	2.87x1.28	759.75	762.5	4.03	843.53	5.39
B4-3	2.81x1.16	881.24	885.13	7.23		
B5-1	2.71x1.22	811.94	984.19	20.03		
B5-2	2.91x1.30	836.27	893.59	4.49	957.13	14.15
B5-3	2.77x1.16	974.68	993.61	17.93		
Forging					827	30

Fig. 7. Engineering stress–strain curves and statistics of the five claddings.

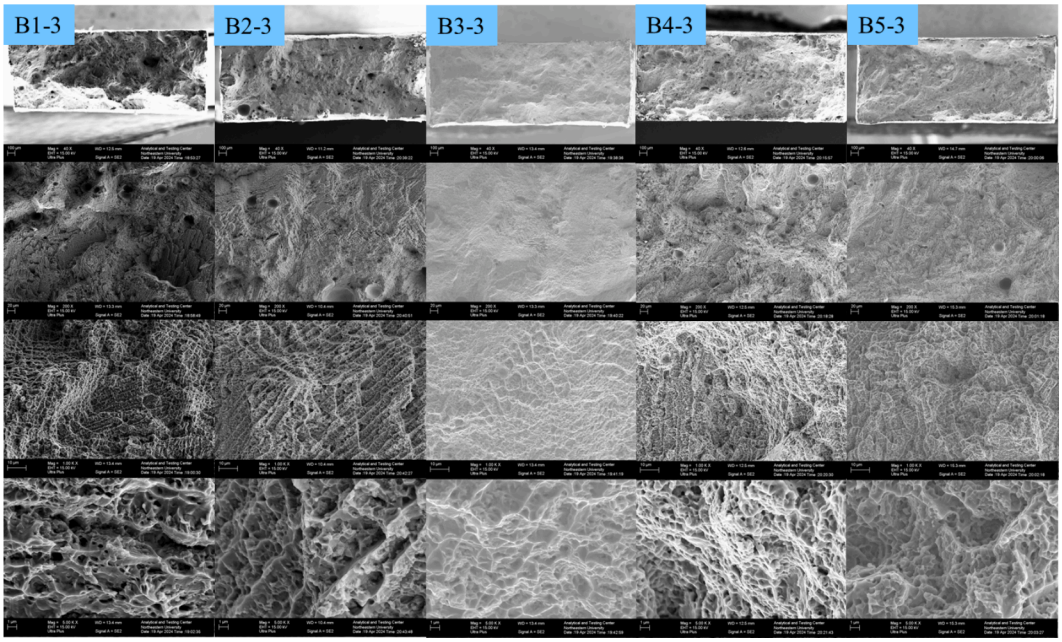

Fig. 8. Morphology of fracture of the five claddings.

resistance of the cladding layer are significantly influenced by the interlayer bonding modes.

1. XRD results: X-ray diffraction results reveal that different interlayer bonding modes have significant effects on the alignment of crystallographic planes and phase formation. In particular, the detection of Nb_6C_5 in B4 and B5 suggests that a rectangle ring interlayer bonding mode may promote the formation of a secondary phase, which could contribute to enhancing the material's hardness.

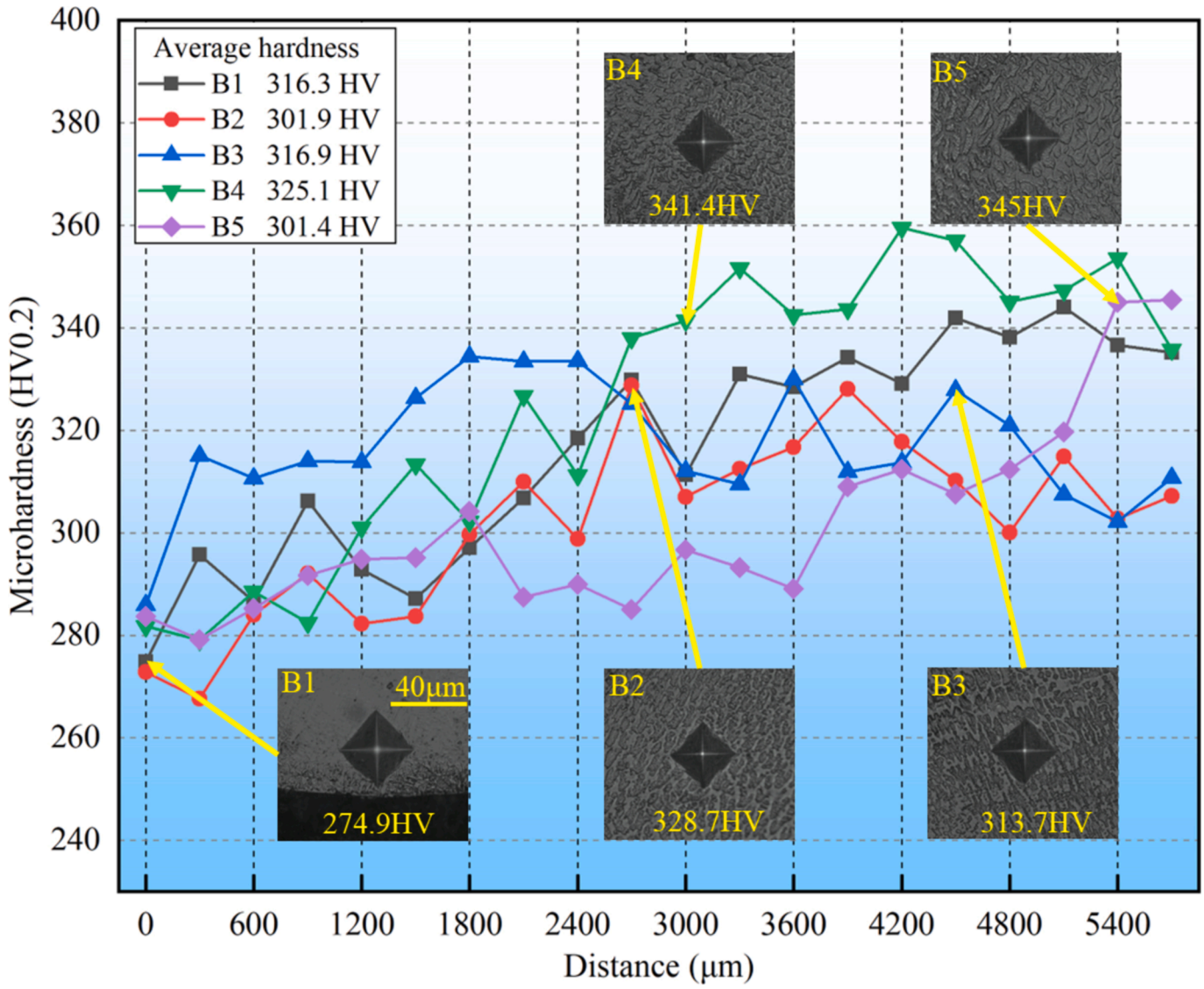

Fig. 9. Microhardness of the five claddings.

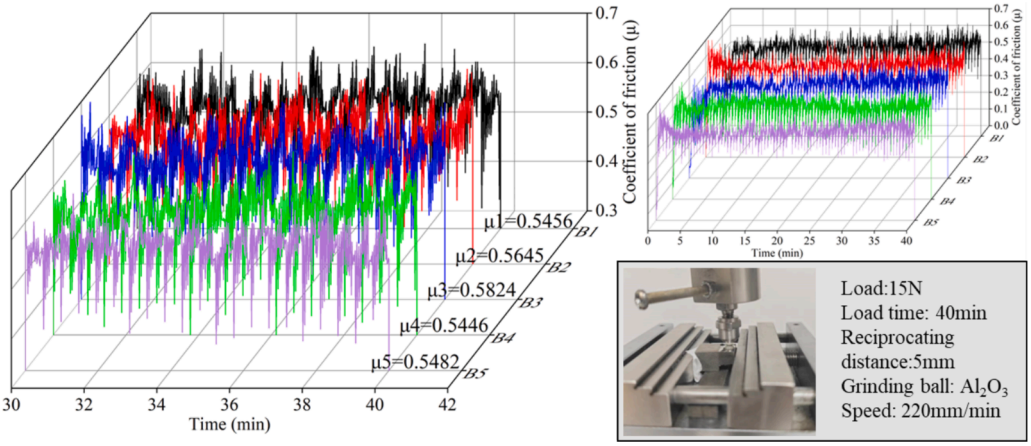

Fig. 10. Coefficient of friction (COF) of the five claddings.

2. Microstructure and composition analysis: EDS analyses show that B4 has a slightly higher Nb content than the other samples, and B3 has the smallest grain size and the most uniform distribution.
3. Mechanical properties: Tensile test results show that B1, B2, and B3 show a ductile fracture, while B4 and B5 show brittle fracture. B3 exhibits the highest average elongation (35.46 %). B5 exhibits the

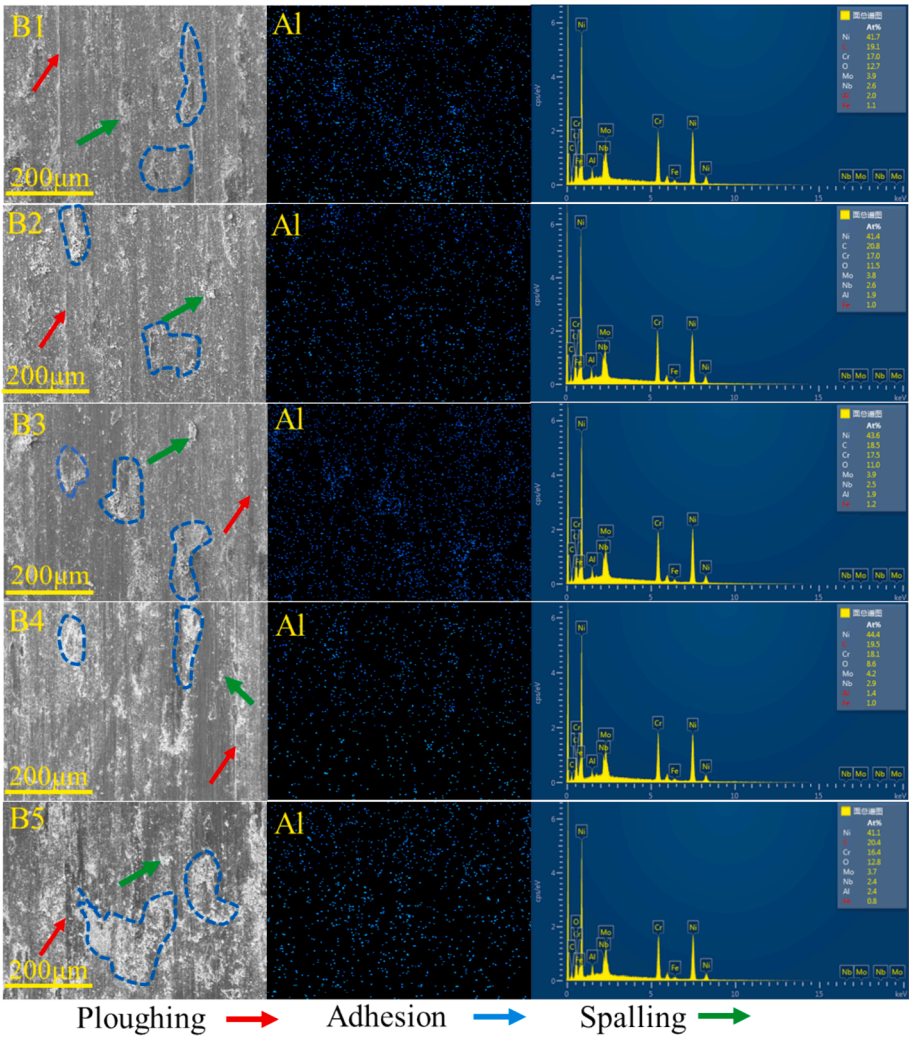

Fig. 11. Wear morphology and EDS analysis results of the five claddings.

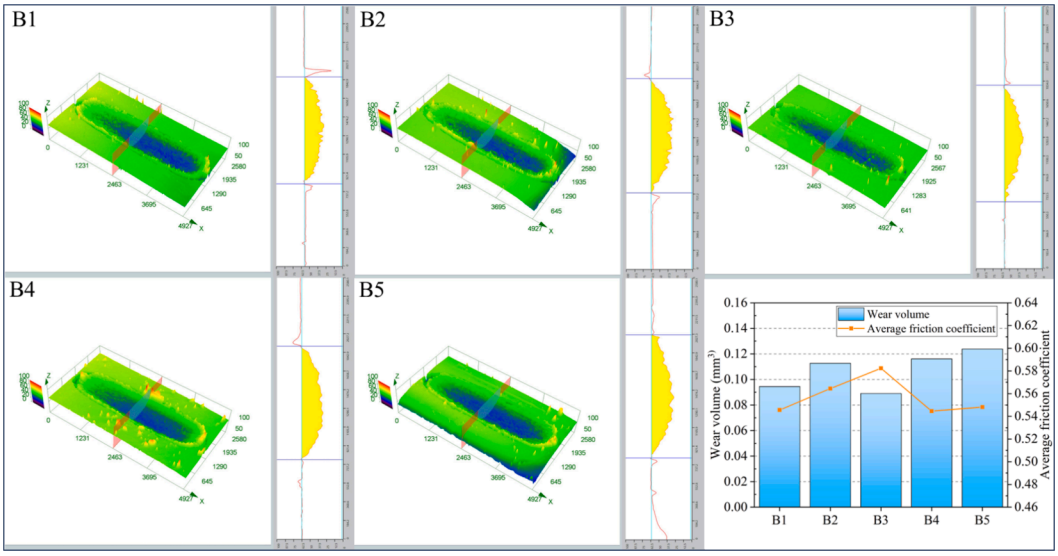

Fig. 12. Wear tracks, scratch depths, and volume loss of the five claddings.

highest average tensile strength (957.13 MPa). In the hardness test results, B4 shows the highest hardness is 325.1HV(0.2).
4. The friction and wear test results show that there are significant differences among different samples, among them, B3 exhibits the smallest wear volume (0.08899 mm^3) and the best overall friction performance.

The results of this study provide a valuable reference for further optimization of laser cladding technology in industrial applications. The properties of the cladding layer can be effectively regulated by selecting appropriate interlayer bonding modes to meet the specific requirements of material properties in specific application environments.

CRediT authorship contribution statement

Yingying Zhang: Writing – review & editing, Writing – original draft, Formal analysis, Data curation, Conceptualization. **Jiayu Sun:** Methodology. **Zhengyu Sun:** Investigation. **Yiqi Wang:** Validation. **Tianbiao Yu:** Project administration, Funding acquisition.

Funding

This work was supported by the National Natural Science Foundation of China [grant number 52075088]; Liaoning Provincial Key Laboratory of Large Equipment Intelligent Design and Manufacturing Technology [grant number 18006001].

Declaration of competing interest

The authors declare that they have no known competing financial interests or personal relationships that could have appeared to influence the work reported in this paper.

Data availability

Data will be made available on request.

References

[1] L. Zhu, P. Xue, Q. Lan, G. Meng, Y. Ren, Z. Yang, P. Xu, Z. Liu, Recent research and development status of laser cladding: a review, Opt. Laser Technol. 138 (2021) 106915, https://doi.org/10.1016/j.optlastec.2021.106915.
[2] X. Kaikai, G. Yadong, Z. Qiang, Comparison of traditional processing and additive manufacturing technologies in various performance aspects: a review, Arch. Civ. Mech. Eng. 23 (3) (2023), https://doi.org/10.1007/s43452-023-00699-3.
[3] Z. Wang, J. Li, Q. Liu, L. Chen, J. Lv, T. Yu, J. Zhao, No-impact trajectory design and fabrication of surface structured CBN grinding wheel by laser cladding remelting method, Opt. Laser Technol. 181 (2025) 111956, https://doi.org/10.1016/j.optlastec.2024.111956.
[4] L. Chen, T. Yu, X. Chen, Y. Zhao, C. Guan, Process optimization, microstructure and microhardness of coaxial laser cladding TiC reinforced Ni-based composite coatings, Opt. Laser Technol. 152 (2022), https://doi.org/10.1016/j.optlastec.2022.108129.
[5] T.B. Yu, L. Yang, Y. Zhao, J.Y. Sun, B.C. Li, Experimental research and multi-response multi-parameter optimization of laser cladding Fe313, Opt. Laser Technol. 108 (2018) 321–332, https://doi.org/10.1016/j.optlastec.2018.06.030.
[6] Y. Zhang, P. Bai, Z. Li, J. Zhang, W. Liu, Multi-objective optimization of laser cladding process parameters for Q345B steel, Mater. Today Commun. 39 (2024), https://doi.org/10.1016/j.mtcomm.2024.108679.
[7] F. Weng, H. Yu, C. Chen, J. Liu, L. Zhao, J. Dai, Z. Zhao, Effect of process parameters on the microstructure evolution and wear property of the laser cladding coatings on Ti-6Al-4V alloy, J. Alloy. Compd. 692 (2017) 989–996, https://doi.org/10.1016/j.jallcom.2016.09.071.
[8] W. Xi, B. Song, Y. Zhao, T. Yu, J. Wang, Geometry and dilution rate analysis and prediction of laser cladding, Int. J. Adv. Manuf. Technol. 103 (9–12) (2019) 4695–4702, https://doi.org/10.1007/s00170-019-03932-7.
[9] F. Bourahima, A.L. Helbert, M. Rege, V. Ji, D. Solas, T. Baudin, Laser cladding of Ni based powder on a Cu-Ni-Al glassmold: influence of the process parameters on bonding quality and coating geometry, J. Alloy. Compd. 771 (2019) 1018–1028, https://doi.org/10.1016/j.jallcom.2018.09.004.
[10] Z. Zhang, D. Wang, G. Liu, Y. Qian, Y. Xu, D. Xiang, Surface modification of 42CrMo steels: a review from wear and corrosion resistance, Coatings 14 (3) (2024) 337, https://doi.org/10.3390/coatings14030337.
[11] F. Xu, Y. Lv, Y. Liu, F. Shu, P. He, B. Xu, Microstructural evolution and mechanical properties of inconel 625 alloy during pulsed plasma arc deposition process, J. Mater. Sci. Technol. 29 (5) (2013) 480–488, https://doi.org/10.1016/j.jmst.2013.02.010.
[12] C.P. Paul, P. Ganesh, S.K. Mishra, P. Bhargava, J. Negi, A.K. Nath, Investigating laser rapid manufacturing for Inconel-625 components, Opt. Laser Technol. 39 (4) (2007) 800–805, https://doi.org/10.1016/j.optlastec.2006.01.008.
[13] L. Du, D. Gu, D. Dai, Q. Shi, C. Ma, M. Xia, Relation of thermal behavior and microstructure evolution during multi-track laser melting deposition of Ni-based material, Opt. Laser Technol. 108 (2018) 207–217, https://doi.org/10.1016/j.optlastec.2018.06.042.
[14] S.P. Kumar, S. Elangovan, R. Mohanraj, J.R. Ramakrishna, A review on properties of Inconel 625 and Inconel 718 fabricated using direct energy deposition, Mater. Today: Proc. 46 (2021) 7892–7906, https://doi.org/10.1016/j.matpr.2021.02.566.
[15] J. Rafiei, A.R. Ghasemi, Development of thermo-mechanical simulation of WC/Inconel 625 metal matrix composites laser cladding and optimization of process parameters, Int. J. Therm. Sci. 198 (2024), https://doi.org/10.1016/j.ijthermalsci.2024.108883.
[16] X. Xu, G. Mi, L. Xiong, P. Jiang, X. Shao, C. Wang, Morphologies, microstructures and properties of TiC particle reinforced Inconel 625 coatings obtained by laser cladding with wire, J. Alloy. Compd. 740 (2018) 16–27, https://doi.org/10.1016/j.jallcom.2017.12.298.
[17] L. Su, T. Xu, X. Ma, G. Mi, L. Wang, Study on the effect of ZrC and CNTs particles on Inconel 625 coatings fabricated by coaxial-wire-feed laser cladding, J. Mater. Res. Technol. 29 (2024) 3934–3945, https://doi.org/10.1016/j.jmrt.2024.02.107.
[18] X. Wang, X. Ren, Y. Xue, B. Luan, Investigation on microstructure and high-temperature wear properties of high-speed laser cladding Inconel 625 alloy, J. Mater. Res. Technol. 30 (2024) 626–639, https://doi.org/10.1016/j.jmrt.2024.02.235.
[19] Y. Zhao, T.B. Yu, J.Y. Sun, L.Y. Chen, Y.D. Chen, Effect of laser cladding on forming microhardness and tensile strength of YCF101 alloy powder in the different full lap joint modes, J. Alloy. Compd. 820 (2020), https://doi.org/10.1016/j.jallcom.2019.04.046.
[20] Y. Zhao, W. Shi, L. Chen, W. Wu, T. Yu, Effect of scanning strategies on anisotropy of YCF104 alloy mechanical properties by laser cladding, Coatings 13 (5) (2023) 842, https://doi.org/10.3390/coatings13050842.
[21] J. Yu, X. Lin, L. Ma, J. Wang, X. Fu, J. Chen, W. Huang, Influence of laser deposition patterns on part distortion, interior quality and mechanical properties by laser solid forming (LSF), Mater. Sci. Eng. A 528 (3) (2011) 1094–1104, https://doi.org/10.1016/j.msea.2010.09.078.
[22] X. Wang, D. Deng, M. Qi, H. Zhang, Influences of deposition strategies and oblique angle on properties of AISI316L stainless steel oblique thin-walled part by direct laser fabrication, Opt. Laser Technol. 80 (2016) 138–144, https://doi.org/10.1016/j.optlastec.2016.01.002.
[23] H. Paydas, A. Mertens, R. Carrus, J. Lecomte-Beckers, J.T. Tchuindjang, Laser cladding as repair technology for Ti–6Al–4V alloy: Influence of building strategy on microstructure and hardness, Mater. Design 85 (2015) 497–510, https://doi.org/10.1016/j.matdes.2015.07.035.
[24] L. Wang, X. Wu, T. Wang, Z. Zhang, X. Jin, X. Xia, Y. Liu, Scanning strategy of multi-layer and multi-track laser cladding for radial grooves of annular thin-walled parts, J. Mater. Eng. Perform. (2024), https://doi.org/10.1007/s11665-023-09078-8.
[25] Y. Zhao, Y. Chen, T. Zhang, T. Yu, Laser fabricated nickel-based coating with different overlap modes, Mater. Manuf. Process. 36 (14) (2021) 1618–1630, https://doi.org/10.1080/10426914.2021.1926490.
[26] L.J. Yang, Y. Wang, M. Djendel, L.T. Qi, Experimental investigation on 3D laser forming of metal sheet, Mater. Sci. Forum 471–472 (2004) 568–572, https://doi.org/10.4028/www.scientific.net/MSF.471-472.568.
[27] T. Petrat, R. Winterkorn, B. Graf, A. Gumenyuk, M. Rethmeier, Build-up strategies for temperature control using laser metal deposition for additive manufacturing, Weld. World 62 (5) (2018) 1073–1081, https://doi.org/10.1007/s40194-018-0604-8.
[28] F. Zafar, O. Emadinia, J. Conceição, M. Vieira, A. Reis, A review on direct laser deposition of inconel 625 and inconel 625-based composites–challenges and prospects, Metals-Basel 13 (4) (2023) 787, https://doi.org/10.3390/met13040787.
[29] G. Muvvala, D. Patra Karmakar, A.K. Nath, In-process detection of microstructural changes in laser cladding of in-situ Inconel 718/TiC metal matrix composite coating, J. Alloy Compd. 740 (2018) 545–558, https://doi.org/10.1016/j.jallcom.2017.12.364.
[30] T. Yu, Y. Zhao, J. Sun, Y. Chen, W. Qu, Process parameters optimization and mechanical properties of forming parts by direct laser fabrication of YCF101 alloy, J. Mater. Process. Tech. 262 (2018), 75e84, https://doi.org/10.1016/.
[31] L. Shu, Z. Heng, P. Li, H. Wu, J. Li, J. Feng, Effect of laser powers on the mechanical properties 27SiMn steel with Inconel 718 cladding coatings, Mater. Res. Express 9 (9) (2022) 96511, https://doi.org/10.1088/2053-1591/ac8f21.
[32] Y. Liu, H. Chen, R. Han, Y. Peng, K. Wang, X. Li, Investigating the microstructure and mechanical properties of 316L/TiB2 composites fabricated by laser cladding additive manufacturing, J. Mater. Res. Technol. 29 (2024) 28–39, https://doi.org/10.1016/j.jmrt.2023.12.261.
[33] M. Feng, T. Lin, G. Lian, C. Chen, X. Huang, Effects of Nb content on the microstructure and properties of CoCrFeMnNiNbx high-entropy alloy coatings by

laser cladding, J. Mater.Research and Technology 28 (2024) 3835–3848, https://doi.org/10.1016/j.jmrt.2024.01.002.
[34] W.T. Zhou, Y. Zhao, C.X. Zhu, Microstructure and wear characteristics of laser-clad CoCrFeMnNiNb0.3 high-entropy alloy coating, J. Mater. Eng. Perform. (2024), https://doi.org/10.1007/s11665-024-09496-2.
[35] L. Chen, Y. Zhao, F. Meng, T. Yu, Z. Ma, S. Qu, Z. Sun, Effect of TiC content on the microstructure and wear performance of in situ synthesized Ni-based composite coatings by laser direct energy deposition, Surf. Coat. Technol. 444 (2022) 128678, https://doi.org/10.1016/j.surfcoat.2022.128678.